JOURNAL OF GEOPHYSICAL RESEARCH, VOL. 105, NO. D17, PAGES 22,211–22,223, SEPTEMBER 16, 2000

# The 2.5 THz heterodyne spectrometer THOMAS: Measurement of OH in the middle atmosphere and comparison with photochemical model results

Christoph R. Englert,[1] Birger Schimpf,[2] Manfred Birk,[2] Franz Schreier,[2]
Michael Krocka,[2] Roland G. Nitsche,[3] and Ruth U. Titz[4]
Institut für Optoelektronik, Deutsches Zentrum für Luft– und Raumfahrt, Oberpfaffenhofen, Germany

Michael E. Summers[5]
E. O. Hulburt Center for Space Research, Naval Research Laboratory, Washington, D. C.

**Abstract.** The interpretation of recent odd hydrogen measurements in the stratosphere from balloons and in the mesosphere from space indicates a serious lack of understanding in atmospheric $HO_x$ chemistry. In order to resolve these persisting problems, coincident measurements of $HO_x$ molecules and/or measurements that cover both altitude regions are desirable. In this work, the airborne 2.5 THz heterodyne spectrometer Terahertz OH Measurement Airborne Sounder (THOMAS) is introduced. Since the first THOMAS measurements in 1994/1995, the spectrometer was significantly improved by modification or replacement of individual components. The THOMAS instrumental setup and properties are presented together with a retrieval algorithm for atmospheric parameters based on a Phillips–Tikhonov regularization scheme. Furthermore, the results of a complete error assessment are given. In August 1997, during the second CRISTA/MAHRSI campaign (Cryogenic Infrared Spectrometers and Telescopes for the Atmosphere / Middle Atmosphere High Resolution Spectrograph Investigation), OH observations were performed by THOMAS covering altitudes between about 30 and 90 km over a full diurnal cycle. Hydroxyl column densities derived from THOMAS measurements are presented and compared to photochemical model results. The model calculations using the standard $HO_x$ chemistry systematically show higher values by about 15 % for the 40–90 km and 50–90 km OH columns. Moreover, a recently proposed change of an $HO_x$ chemistry reaction rate is included into the comparison which, for the same altitude intervals, yields OH column densities that are about 10 % lower than the THOMAS measurements. A detailed comparison of the THOMAS and MAHRSI measurements is presented in a seperate publication [*Englert et al.*, 2000].

## 1. Introduction

Ozone chemistry throughout the middle atmosphere (stratosphere and mesosphere) is closely connected to the odd hydrogen family ($HO_x$ = H, OH, $HO_2$). A detailed understanding of atmospheric chemistry involving odd hydrogen is therefore of great importance for the refinement of atmospheric models that enable us to understand the current state of the atmosphere and possible future changes. Comparing photochemical model results to measurements is a rigorous test of the current understanding of atmospheric chemistry. However, measuring these radicals with sufficient precision and accuracy poses an experimental challenge. Owing to major advances in the development of suitable in situ and remote sensing techniques, a number of instruments have supplied valuable data in the last decades.

Balloon–borne measurements of OH concentration profiles in the middle and upper stratosphere have been performed using Lidar [*Heaps and McGee*, 1983, 1985], infrared Fourier transform spectrometry [*Carli and Park*, 1988; *Carli et al.*, 1989; *Park and Carli*, 1991; *Johnson et al.*, 1995], ultraviolet spectrometry [*Torr et al.*, 1987], and infrared Fabry–Pérot spectrometry [*Pickett and Peterson*, 1993]. A comparison of some results can be found [e.g.,

[1]Now at E. O. Hulburt Center for Space Research, Naval Research Laboratory, Washington, D. C.

[2]Now at Remote Sensing Technology Institute, Deutsches Zentrum für Luft– und Raumfahrt e.V., Oberpfaffenhofen, Weßling, Germany.

[3]Now at Intelligente Systemautomatisierung (ISA) Industrieelektronik, Weiden, Germany.

[4]Now at Institut für Weltraumsensorik und Planetenerkundung, Deutsches Zentrum für Luft– und Raumfahrt e.V., Berlin, Germany.

[5]Now at School of Computational Sciences, Department of Physics and Astronomy, and Center for Earth Observing and Space Research, George Mason University, Fairfax, Virginia.



Paper number 2000JD900305.
0148-0227/00/2000JD900305$09.00

# Report Documentation Page

*Form Approved*
*OMB No. 0704-0188*



| 1. REPORT DATE | 2. REPORT TYPE | 3. DATES COVERED |
|---|---|---|
| **SEP 2000** | | **00-00-2000 to 00-00-2000** |

| 4. TITLE AND SUBTITLE | 5a. CONTRACT NUMBER |
|---|---|
| **The 2.5 THz heterodyne spectrometer THOMAS: Measurement of OH in the middle atmosphere and comparison with photochemical model results** | 5b. GRANT NUMBER |
| | 5c. PROGRAM ELEMENT NUMBER |
| 6. AUTHOR(S) | 5d. PROJECT NUMBER |
| | 5e. TASK NUMBER |
| | 5f. WORK UNIT NUMBER |
| 7. PERFORMING ORGANIZATION NAME(S) AND ADDRESS(ES)<br>**Naval Research Laboratory,E. O. Hulburt Center for Space Research,4555 Overlook Avenue SW,Washington,DC,20375** | 8. PERFORMING ORGANIZATION REPORT NUMBER |
| 9. SPONSORING/MONITORING AGENCY NAME(S) AND ADDRESS(ES) | 10. SPONSOR/MONITOR'S ACRONYM(S) |
| | 11. SPONSOR/MONITOR'S REPORT NUMBER(S) |

12. DISTRIBUTION/AVAILABILITY STATEMENT
**Approved for public release; distribution unlimited**

13. SUPPLEMENTARY NOTES

14. ABSTRACT
**see report**

15. SUBJECT TERMS

| 16. SECURITY CLASSIFICATION OF: | | | 17. LIMITATION OF ABSTRACT | 18. NUMBER OF PAGES | 19a. NAME OF RESPONSIBLE PERSON |
|---|---|---|---|---|---|
| a. REPORT | b. ABSTRACT | c. THIS PAGE | | | |
| **unclassified** | **unclassified** | **unclassified** | **Same as Report (SAR)** | **13** | |

*Pickett and Peterson*, 1993]. Time–dependant $HO_x$ profiles of the middle stratosphere resulting from a balloon–borne infrared spectrometer experiment were presented for the first time by *Chance et al.* [1996]. The $HO_x$ distribution was found to largely agree with the standard photochemical model except for OH at the highest measurement altitudes near 38 km which was significantly higher ($\approx$ 33% or 3 $\sigma$ measurement uncertainty) than the model values. (Descriptions of photochemical models are given by *Siskind et al.* [1995], *Pickett and Peterson* [1996], *Salawitch et al.* [1994], *Clancy et al.* [1994], or *Sandor and Clancy* [1998].) *Pickett and Peterson* [1996] reported stratospheric OH concentration profiles retrieved from balloon–borne far–infrared limb observations of a triple Fabry–Pérot interferometer. The observations cover full diurnal cycles and basically agree well with the applied photochemical model. However, the comparison of a data set from *Pickett and Peterson* [1996] with a different model shows an OH underestimation of about 20 % ($\approx 2\,\sigma$ measurement uncertainty) at 37 km [*Ostermann et al.*, 1997]. Long–term ground–based total column measurements have been reported by *Burnett and Minschwaner* [1998]. They observe significant changes in total column OH during the last 2 decades. Since tropospheric OH is only a minor contribution to the total column, they conclude that these changes are most likely originating from changes in stratospheric or mesospheric OH. However, the measured OH column abundance is significantly higher than that predicted from standard chemistry.

Hydroxyl measurements in the mesosphere from a space platform have been performed with the Middle Atmosphere High Resolution Spectrograph Investigation (MAHRSI) in 1994 [*Conway et al.*, 1996] and 1997. The reported OH concentration profiles are inconsistent with model calculations using the standard photochemistry (later referred to as model A). Two alternative changes to standard chemistry were proposed to explain the MAHRSI observations [*Summers et al.*, 1997]. Either a 50 % reduction of the $k_1$ rate coefficient for

$$O + HO_2 \rightarrow OH + O_2 \qquad (1)$$

(later referred to as model B) or a 20 % reduction in the rate coefficient $k_1$ together with a 30 % increase in the $k_2$ rate coefficient for

$$OH + HO_2 \rightarrow H_2O + O_2 \qquad (2)$$

lead to consistency of OH model results and observations. Compared to the standard model, this rate constant reduction also resulted in a substantially better agreement between the model ozone concentration and simultaneous ozone measurements at 50 km by Cryogenic Infrared Spectrometers and Telescopes for the Atmosphere (CRISTA). Ground–based observations of lower mesospheric $HO_2$ [*Sandor and Clancy*, 1998] favor the reduction of $k_1$ only. This modification of the $HO_x$ chemistry has only a minor effect on lower stratospheric OH, $HO_2$, and $O_3$ abundances [*Sandor and Clancy*, 1998; *Summers et al.*, 1997; *Chen et al.*, 1997]. However, a change of $k_1$ by 50 % would mean a change of more than two $\sigma$ measurement uncertainty and has been opposed by the laboratory and stratospheric modeling community [cf. *Sandor and Clancy*, 1998]. The MAHRSI data also corroborate the existance of an unexplained $H_2O$ layer between 65 km and 70 km observed by the Halogen Occultation Experiment (HALOE) [*Summers et al.*, 1997; *Siskind and Summers*, 1998].

Simultaneous measurements of OH, $HO_2$, $H_2O$, and $O_3$ in the upper stratosphere have recently been reported by *Jucks et al.* [1998]. Above 35 km they found OH concentrations in agreement with standard chemistry, while the observed $HO_2$ concentrations showed about 25 % higher values than the standard model. The enhanced $HO_2$ abundance seems to be consistent with the mesospheric $HO_2$ observations of *Sandor and Clancy* [1998]. The measurements reported by *Jucks et al.* [1998] imply a higher total $HO_x$ concentration as well as a difference in the partitioning of OH and $HO_2$. In conclusion, the present set of $HO_x$ observations neither shows general mutual agreement nor good agreement with standard model calculations.

In August 1997, during the second MAHRSI mission, the 2.5 THz OH Measurement Airborne Sounder (THOMAS) performed vertical sounding measurements of OH between about 30 km and 90 km. The geometry of the observations was chosen in a way that they coincided in space and time with MAHRSI measurements whenever possible, thus allowing a direct intercomparison. Together with THOMAS, the Fast In Situ Stratospheric Hygrometer (FISH) [*Zöger*, 1996] was operated on board the Deutschen Zentrum für Luft– und Raumfahrt (DLR) research aircraft FALCON and supplied simultaneous water vapor data at flight altitude for most of the THOMAS observations.

The next section of this paper presents some fundamentals of far–infrared spectroscopy. The THOMAS instrument and the measurement conditions are described in the following section with emphasis on the major improvements of the instrument made after the first flights of THOMAS in 1994 [*Titz et al.*, 1995a] and 1995 [*Titz et al.*, 1995b]. The inversion algorithm is outlined in section 4 together with an assessment of possible errors in the experimental data as well as in the inversion of OH concentration profiles from the measured far–infrared emission spectra. In sections 5 and 6 the inversion results are shown and compared to model calculations. A detailed comparison to results from the second MAHRSI campaign is presented in a seperate publication [*Englert et al.*, 2000].

## 2. Far–Infrared Thermal Emission of Atmospheric OH

In a feasibility study by *Miller et al.* [1992] the pure rotational transitions of OH at 2.5 THz (83 $cm^{-1}$) were found to be suitable for measuring vertical OH profiles with an airborne, uplooking heterodyne receiver flying at altitudes above the tropopause in order to reduce signal attenuation by water vapor absorption. The double side band receiver THOMAS observes these thermal emission lines of OH in the lower side band superimposed with an $H_2O$ transition at 84.456 $cm^{-1}$ in the upper side band that provides information about the $H_2O$ abundance.

The radiance $I$ at wavenumber $\nu$ received by THOMAS is described by the radiative transfer equation. Its integral form, neglecting scattering and assuming local thermodynamic equilibrium, is given by [*Liou*, 1980]

$$I(\nu) = I_\infty(\nu)\,\mathcal{T}(\nu,\infty) - \int_z^\infty dz'\, B\big[\nu,T(z')\big]\,\frac{\partial\mathcal{T}(\nu,z')}{\partial z'}\,, \quad (3)$$

where $B$ is the Planck function at temperature $T$ and $I_\infty$ is a background contribution, for example, the 3 K background radiation of deep space. The monochromatic transmission $\mathcal{T}$ (relative to the observer at $z$) is given according to Beer's law by

$$\mathcal{T}(\nu,z') = \exp\left[-\int_z^{z'} \left(\sum_m k_m^r(\nu,z'')\,n_m(z'') + \alpha_m^c(\nu,z'')\right) dz''\right], \quad (4)$$

where $n_m$ is the number density of molecule $m$ and $k_m^r$ is its absorption cross section for resonant absorption. The continuum absorption due to nonresonant effects is denoted by the continuum absorption coefficient $\alpha_m^c$. Note that the absorption cross section and the absorption coefficient depend on pressure and temperature, but for brevity we use the condensed notation $k_m^r(\nu,z) \equiv k_m^r\big[\nu,p(z),T(z)\big]$. For simplicity, we have assumed a vertical path geometry, but (3) and (4) are easily generalized to arbitrary slant paths. Instrument influences on the measured spectrum are not considered in equation (3).

### 2.1. Resonant and Nonresonant Absorption

For an individual line $l$ the spectral absorption cross section $k_{m,l}^r$ is the product of the temperature–dependent line strength $S_{m,l}(T)$ and a normalized line shape function $b$ describing the broadening mechanism, $k_{m,l}^r(\nu,z) = S_{m,l}(T)\,b\big[\nu,\nu_{m,l},\gamma_{m,l}(p,T)\big]$, where $\nu_{m,l}$ is the line center and $\gamma_{m,l}$ is the line width. In general, the absorption cross section is obtained by summing over the contributions from many lines, $k_m^r = \sum_l k_{m,l}^r$. For the far–infrared and under atmospheric conditions, the combined effect of pressure broadening (corresponding to a Lorentzian line shape) and Doppler broadening (corresponding to a Gaussian line shape) can be represented by a Voigt line profile.

Nonresonant absorption is described by an absorption coefficient $\alpha_m^c$ showing a weak wavenumber dependence. In the spectral region observed by THOMAS the $H_2O$ continuum and the $N_2$ continuum are dominant [*Bühler et al.*, 1996; *Urban*, 1998]. The semiempirical $H_2O$ continuum described by *Clough et al.* [1989] is a pure far wing continuum correcting the contribution of lines more than 25 $cm^{-1}$ away from the spectral region of interest. *Liebe et al.* [1993] formulated an empirical expression for the continuum contribution of collision induced $N_2$ absorption. Because of the lack of experimental data in the spectral region of interest, modeling these continua is connected with high uncertainties. Especially the $N_2$ continuum is less established than the $H_2O$ continuum, but its application yields better agreement between measured spectra and radiative tranfer calculations. Figure 1 shows both continua calculated for the Air Force Geophysics Laboratory (AFGL) U.S. standard atmosphere [*Anderson et al.*, 1986]. In wide regions of the atmosphere the $N_2$ continuum is dominant except for altitudes near the flight altitude of THOMAS, where both continua are similar in magnitude. The $H_2O$ continuum is proportional to the $H_2O$ concentration. At flight altitudes of the THOMAS instrument near the tropopause, where the $H_2O$ concentration is exponentially decreasing with increasing altitude, the $H_2O$ concentration is highly variable, and the $H_2O$ continuum becomes dominant in regions of high $H_2O$ concentration. The main influence of the continua on the OH lines is due to damping of the signal by the continuum absorption on the first few kilometers above the observer height.

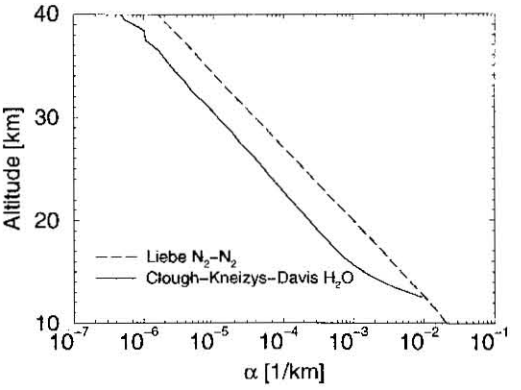


**Figure 1.** Comparison of $H_2O$ and $N_2$ continuum absorption coefficients

### 2.2. Spectral Information Contents for Retrieval

Spectral information about the OH concentration profile can be found in the line shape of the OH lines. For altitudes lower than 50 km, where pressure broadening is dominant for OH, the line width of the emission lines decreases with increasing altitude. The pressure broadening line width is proportional to the pressure and ranges from $2\times10^{-2}$ $cm^{-1}$ at flight altitude to $1\times10^{-4}$ $cm^{-1}$ at 50 km. As a consequence, the line profile has to be completely resolved to allow the retrieval of altitude information. Above 50 km the nearly altitude–independent Doppler broadening becomes dominant so that the line shape of the OH lines contains information about the mesospheric column only.

## 3. Improved THOMAS Instrument

The THOMAS instrument is a further development of a 2.5 THz heterodyne spectrometer of the Max–Planck–Institute for Radioastronomy in Bonn, Germany, where it was built for astronomical research on board the Kuiper Airborne Observatory [*Röser*, 1991]. THOMAS is a similar spectrometer, modified for atmospheric measurements using the DLR research aircraft FALCON. After two campaigns in 1994 and 1995, major components of THOMAS have been optimized or replaced to improve the spectrometers performance.

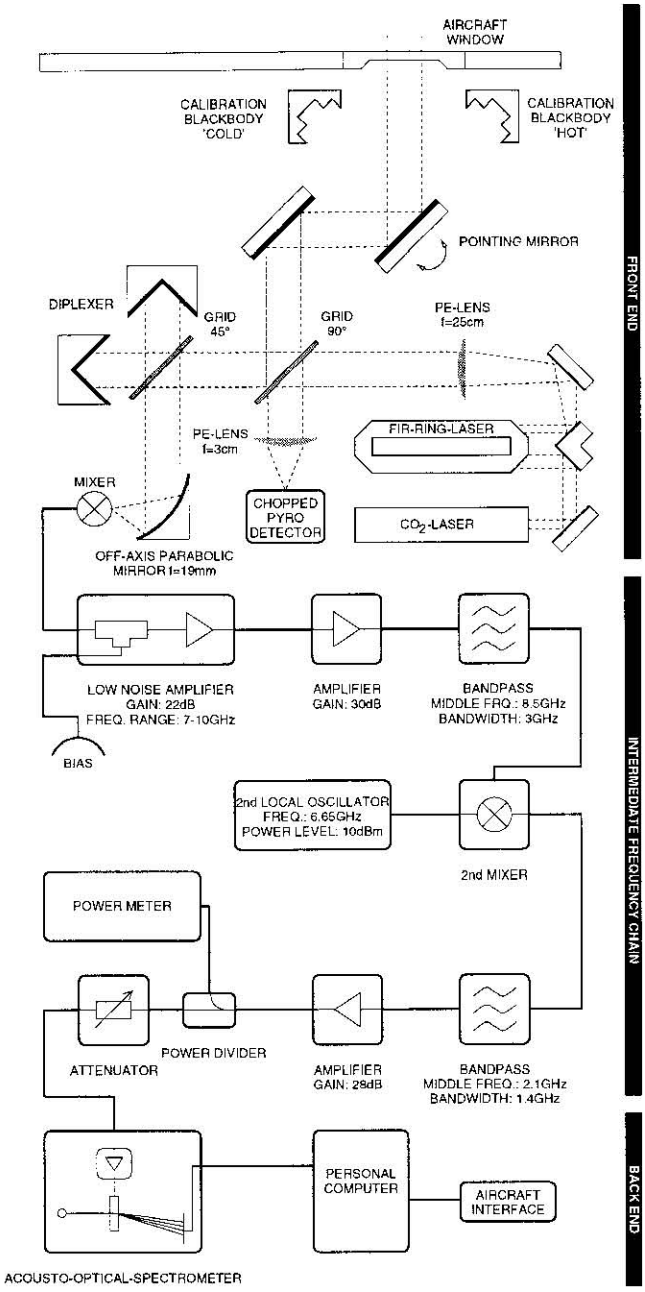


**Figure 2.** Schematic drawing of the THOMAS instrument

Figure 2 shows a schematic of the THOMAS instrument. The atmospheric signal enters the fuselage through a special aircraft window. After being reflected by the pointing mirror and a plane mirror, one half of the unpolarized radiation gets reflected into the diplexer by the 90° wire grid. About 90 % of the monochromatic radiation of the first local oscillator (LO), a $CO_2$ laser pumped methanol laser ($\nu_{LO}$ = 84.15095 $cm^{-1}$) is transmitted by the 90° wire grid into the diplexer. The remaining fraction is reflected and detected by a chopped pyroelectrical detector to monitor the LO performance. The diplexer rotates the polarization of the first LO to the polarization of the atmospheric signal. The combination of the first LO beam and the atmospheric radiation is focused onto an open structure corner cube mixer by an off–axis parabolic mirror. The actual mixer consists of a whisker antenna contacting a honeycomb Schottky diode. The diode type T23, supplied by the University of Virginia, was used for this work [*Crowe et al.*, 1992]. The resulting double side band (DSB) spectrum around 8.5 GHz is amplified and mixed down to a center frequency of 2.1 GHz (bandwidth: 1.4 GHz) by the intermediate frequency chain (IF chain). An acousto optical spectrometer (AOS) is used to perform a spectral analysis of the signal. The resulting spectra are displayed and stored by a personal computer. The computer also stores data from the aircraft interface like altitude, roll and pitch angle, outside temperature, and heading as well as instrumental housekeeping data like $CO_2$ laser power, methanol laser power, mixer voltage, temperatures of the window, the hot and cold reference black bodies, and the total power leaving the IF chain. The radiometric calibration of the spectra is performed using spectra of the two reference black bodies at liquid nitrogen and ambient temperature.

Critical components and parameters of THOMAS instrument are discussed in the following, including the modifications that were made since the 1994/1995 flights.

### 3.1. Quasi–Optical Design

The quasi optics of the front end of THOMAS has been designed for a beamwaist of 9 mm corresponding to a Rayleigh length of 2.157 m and an asymptotic field of view angle of 0.24°. The defacto field of view depends on the whisker position in the corner cube structure of the mixer, the position of the mixer relative to the parabolic mirror, and the qualitiy of the wire grids (compare with section 3.3). For the atmospheric measurements the mixer position was adjusted for maximum reception of the first LO. An adjustment of the whisker position was not possible during operation of the mixer. Since the field of view is not as critical for a vertical sounding instrument like THOMAS compared to limb sounding experiments, this adjustment procedure was considered to be sufficient (see also section 4.2). Because of the narrow field of view in combination with the uplooking geometry, a pencil beam was assumed for the retrieval of OH concentrations.

### 3.2. Aircraft Window

For the earlier atmospheric measurements with THOMAS a polyethylene (PE) aircraft window had been used [*Titz et al.*, 1995a]. The transmittance of the PE aircraft window was only 61 %, and a proper temperature measurement of the window was difficult because of the low thermal conductivity of PE that caused large temperature gradients in the window during the flight. Because of these disadvantages, the polyethylene aircraft window was replaced by an antireflection–coated, wedged, single–crystal silicon window [*Englert et al.*, 1999a]. The free aperture of the new window is 5 cm × 15 cm allowing pointing angles between 5° and 20° toward horizontal. The temperature of the new window, which is needed to account for the far–infrared radiation emitted by the window, can be measured more accurately due to the much higher thermal conductivi-

ty of silicon. Moreover, the absorption coefficient of silicon in the far–infrared is significantly lower, making the window more transparent. Laboratory measurements showed that the transmittance of new window is about 89 %. The losses can be divided into about 7 % reflection losses and about 4 % losses due to absorption. However, the transmittance of the window decreased up to about 20 % while it was illuminated by direct sunlight during the measurement flights. Temperature changes of the window, typically of the order of 2 K, can be ruled out as a reason for the transmittance change. Laboratory measurements with THOMAS and with a Fourier transform spectrometer [*Englert et al.*, 1999b] confirmed that the change in absorption is due to an increased number of electrons in the semiconductor's conduction band. The source of the additional free charges in the silicon are transitions of electrons from the valence band to the conduction band caused by radiation with energies greater than the bandgap (visible light, UV).

A correction of the photon induced absorption was determined using two successive airborne measurements, one with and one without direct sunlight illuminating the window. These particular measurements have been selected from all available spectra because the coinciding in situ water vapor measurements of the FISH instrument aboard the FALCON showed that the flight altitude was well above the tropopause for this day. Therefore the effect on the measured spectrum due to changing water vapor abundance in the first few kilometers of the line of sight is expected to be minimal, and the observed change in signal absorption can be attributed to photon induced absorption only. The absorption change of the window was basically determined by fitting the window absorption so that the shapes of the measured water vapor emission lines matched best. This procedure assumes identical distribution of middle atmospheric water vapor for both measurements.

Figure 3 shows the two spectra measured with and without the Sun shining directly onto the window. In the upper panel of Figure 3 the raw spectra are displayed, whereas in the lower panel the window corrected spectra are shown. The predominant features in the spectra are a rotational line of water vapor at about 84.456 $cm^{-1}$ in the upper side band and a rotational line triplet of hydroxyl around 83.869 $cm^{-1}$ in the lower side band.

All the measured spectra have been window corrected under the assumption of a linear relation between the additional absorption and the solar energy flux in the visible and UV at the window. The diffuse solar energy flux in the shade was estimated to be 10 % of the direct radiation of the Sun.

### 3.3. Wire Grids

Laboratory measurements of the THOMAS far–field antenna pattern showed that it suffers significant distortion when reflected by the 90° wire grid (wire diameter: 10 $\mu$m; specified wire spacing: $d$=25 $\mu$m). This effect was due to large tolerances in the spacing of the grid ($0\,\mu m \leq d \leq 80\,\mu$m). The tungsten wire grids have been replaced by new grids with a smaller tolerance in the grid spacing ($0\,\mu m \leq d \leq 40\,\mu$m), thus improving the beam pattern.

### 3.4. First Local Oscillator

Power stability and especially frequency stability is needed for the first LO. The stability of the FIR laser power is maintained by the electronic adjustment of the $CO_2$ laser resonator length, keeping the diode voltage, which is depending on the LO power, at a constant value. No frequency stabilization of the first LO is used. Measurements on board the aircraft as well as in the laboratory showed that the maximum change in LO frequency, mostly due to thermal expansion of the FIR laser resonator, is of the order of 2 MHz ($\approx 6.7\times10^{-5}\,cm^{-1}$). Note that a drift in frequency of the first LO causes a broadening of the instrumental line shape function (ILS).

### 3.5. Diplexer Adjustment

A position adjustment of one roof top mirror of the diplexer was performed immediately after takeoff for every flight. The adjustment was done by maximizing the diode voltage, thus maximizing the transmittance of the first LO. The maximum uncertainty of the adjustment was of the order of 2 % in diode voltage resulting in a sideband ratio of $1.00 \pm 0.08$. For a misaligned diplexer the sideband ratio remains unity at the center frequency of the spectrum and increases/decreases toward the lower/upper end of the spectrum. Sideband ratios inferred from laboratory measurements of methanol emission lines gave no indication of any major additional sideband ratio variations, for example, due to changing mixer properties.

### 3.6. First Mixer and Low–Noise Amplifier

A quasi–optical mixer structure introduced by *Röser* [1991] was used for the measurements reported here. The liquid nitrogen cooled low noise amplifier (LNA) was re-

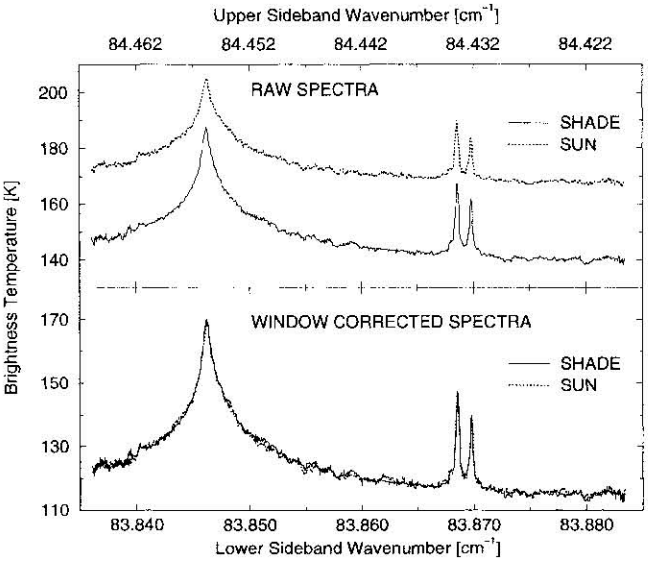


**Figure 3.** (top) Raw, radiometric calibrated spectra. The dotted spectrum was measured while the Sun was shining directly onto the aircraft window. The solid line spectrum was observed while the aircraft window was in the shade. (bottom) Window corrected spectra.

placed by a significantly smaller amplifier unit that can be operated at room temperature without any performance reduction of the spectrometer [*Nitsche*, 1998].

### 3.7. Intermediate Frequency Chain

The IF chain consists of standard microwave components except for the LNA mentioned above. Figure 2 shows the individual devices. After the second mixer stage, a power meter is used to measure the relative power entering the AOS (middle frequency: 2.1 GHz, bandwidth: 1.4 GHz) during all the atmospheric and reference black body observations. The noise temperature of the IF chain was 144 K.

### 3.8. Acousto Optical Spectrometer

Changes in the optics of the AOS and a new readout and data processing unit significantly improved the performance of the AOS that was used together with THOMAS in the 1995 campaign. Subsequent spectral averaging over three CCD pixels was used to minimize the influence of speckles and to increase the signal to noise ratio. The resulting full halfwidth of the instrumental line shape function was reduced to about 3 MHz. The influence of a possible frequency drift of the first LO by about 2 MHz (compare with section 3.4) translates to a variation of the half width half maximum of the final ILS by about 0.2 MHz (compare with Table 1.). The spectral variation of the ILS was neglected regarding the influence of the first LO on the ILS.

### 3.9. Calibration

The atmospheric spectral radiance cannot be measured directly by submillimeter spectrometers. Instead, a spectral noise equivalent power (NEP) is measured which is the sum of the $NEP_{rec}$ (receiver noise equivalent power) and the $NEP_{sig}$ (signal noise equivalent power). The atmospheric NEP measurement has to be calibrated to obtain the desired spectral radiance. This can be done using measurements of two reference blackbodies with known temperature. The calibration procedure makes use of the constancy of $NEP_{rec}$ as well as the linear relation between $NEP_{sig}$ and the detected radiance. (The linearity of the instrument response was investigated using laboratory measurements of methanol emission lines.) In other words, the stability of the instrument is needed. To obtain a minimum uncertainty in the calibrated spectrum, the temperatures of the reference blackbodies have to be choosen in a way that the unknown (atmospheric) radiance lies between the radiances emitted by the two blackbodies. The optimal ratio of integration intervals for the three individual measurements depends on the blackbody temperatures and the atmospheric radiance [*Klein*, 1993]. It can be shown that for the above mentioned conditions, the signal–to–noise ratio of the calibrated spectrum is independent of the blackbody temperatures. For the measurements presented in this work the standard measurement sequence (hot–atmosphere–cold–atmosphere...) has been chosen with the following integration intervals: $t_{hot}$ = 1.5 s, $t_{atm}$ = 2.0 s, and $t_{cold}$ = 2.5 s. These time periods have been selected under consideration of the system stability and the time required to turn the pointing mirror. The system stability (compare with section 3.10) asks for short integration times so that instrument drifts can be neglected. On the other hand, short integration intervals require frequent turning of the pointing mirror which consumes valuable measurement

**Table 1.** Summary of Error Sources and Their Effect on the Weighted OH Column Densities

| Parameter | Estimated Magnitude of Variation | Error in Weighted OH Column | | |
|---|---|---|---|---|
| | | 30–50 km | 50–90 km | 40–90 km |
| Gaussian noise (s. d.) | 0.75 K | $1.6\times10^{12}$ cm$^{-2}$ | $1.6\times10^{12}$ cm$^{-2}$ | $2.3\times10^{12}$ cm$^{-2}$ |
| Regularization parameter $\lambda_{OH}$ | +100%/-50% | 15.0% | 5.7% | 6.6% |
| $c_{H_2O}/c_{OH}$ ratio | +100%/-50% | 13.0% | 4.4% | 1.4% |
| Temperature profile bias | 5 K | 1.1% | 3.5% | 3.1% |
| Ozone profile | 20% | 2.8% | $\ll 1\%$ | $\ll 1\%$ |
| Pressure profile (altitude shift) | 13% | 8.0% | 4.4% | 4.0% |
| $H_2O$ variation at observer | $10 \rightarrow 30$ ppm | 2.0% | $\ll 1\%$ | 0.3% |
| $N_2$ continuum absorption | 50% | 4.2% | 2.2% | 1.4% |
| $H_2O$ continuum absorption | 50% | 2.8% | 1.3% | 0.9% |
| $H_2O$ pressure broadening parameter | 15% | 4.3% | $\ll 1\%$ | $\ll 1\%$ |
| OH triplet line strength | 1% | 1.0% | 1.0% | 1.0% |
| OH pressure broadening parameter | 4% | $\ll 1\%$ | 1.3% | 1.1% |
| OH pressure broadening exponent | 20% | 0.4% | 0.9% | 1.1% |
| Spectrum baseline offset | 3 K | 5.6% | 6.6% | 5.3% |
| Sideband ratio | 8% | 3.0% | 5.6% | 4.6% |
| Window transmittance | 2% | 4.9% | 2.1% | 1.7% |
| ILS width | 0.2 MHz | 1.0% | 0.9% | 0.3% |
| AOS nonlinearity correction | 0.1 | 3.5% | 4.0% | 4.0% |
| Pointing bias | 1° | 5.4% | 7.0% | 6.3% |
| Root mean square of relative and systematic errors | | $\approx$24% | $\approx$15% | $\approx$14% |

time. For this work, the spectra have been calibrated with a procedure similar to the "weighted calibration" reported by *Crewell* [1993]. This method uses two hot and cold observations (one preceding and one following the atm measurement) for the calibration of a single atmospheric spectrum, thus canceling out linear instrumental drifts. Consecutive calibrated spectra have been averaged to obtain a higher signal–to–noise ratio. Here the individual spectra have been averaged to give a total measurement time of 20 min or more for a final spectrum.

### 3.10. System Stability

Stability is a key property of a heterodyne spectrometer because it is required to determine the timing of the measurements. As mentioned above, three measurements are needed to derive a calibrated spectrum (compare with section 3.9). During the time the three data sets are acquired, total system stability is desired. The Allan variance is commonly applied to investigate the stability of submillimeter spectrometers [*Stanley*, 1994; *Allan* 1966]. Allan variances have been calculated for a THOMAS airborne measurement using only the observations of the cold reference blackbody. The total measurement time was about 1 hour. The results for three spectral channels corresponding to pixels of the AOS charge–coupled device (CCD) and for the integral total power measurements are depicted in Figure 4.

Minima of the Allan variance indicate the number of measurements that can be averaged without significant influence of instrument drifts on the averaged measured value. Said differently, they determine the maximum interval of stability. Figure 4 shows that for this measurement stability was accomplished for a longer time than the period between two

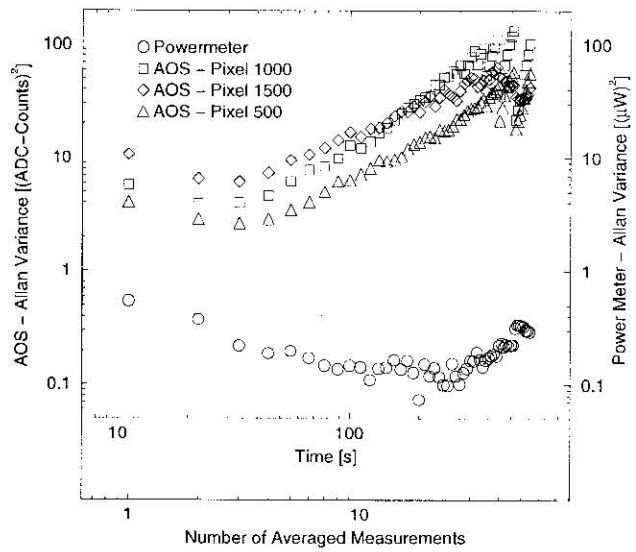


**Figure 4.** Allan variances for three CCD pixels (pixel 500, close to water vapor line center; pixel 1000, center of CCD; and pixel 1500, close to OH lines) and for total power measurements. Only observations of the cold reference blackbody during a flight measurement have been used for the calculation. The given time corresponds to the number of measurements multiplied by the time between the beginnings of two consequtive measurements.

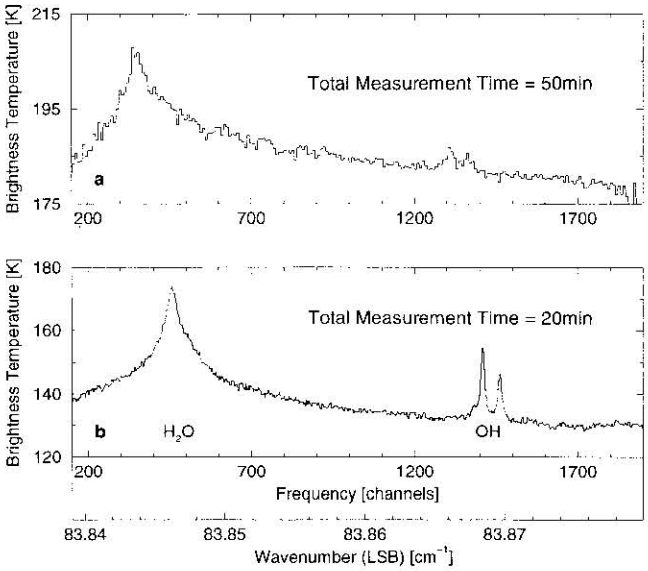


**Figure 5.** (a) Spectrum measured with THOMAS during the Second European Stratospheric Arctic and Midlatitude Experiment (SESAME) campaign 1995 [*Titz et al.*, 1995b]. Eight frequency channels have been averaged. (b) Spectrum measured with the improved THOMAS during the CRISTA/MAHRSI campaign 1997. Three frequency channels have been averaged. (The bandwidth of one frequency channel corresponding to a CCD pixel is about 0.7 MHz.) The wavenumber scale is given for the lower side band (LSB) of the lower panel.

"cold measurements" which is the minimum requirement for a calibration procedure that assumes system stability (compare with section 3.9).

### 3.11. System Sensitivity

The performance of an ideal submillimeter spectrometer can be characterized by the receiver noise temperature (RNT). Together with the measurement time and the spectral resolution, the RNT determines the sensitivity of an ideal spectrometer [*Kraus*, 1966]. The value of the RNT can easily be calculated with the Y factor method [*Hachenberg and Vowinkel*, 1982] using measurements of the hot and cold blackbody. The RNT values achieved by THOMAS during the flights have been around 12,000 K (DSB) at the IF chain output.

The sensitivity of a real submillimeter spectrometer is decreased by additional noise contributions like amplifier fluctuations or non–Gaussian noise originating in the first mixer unit. For the 1997 THOMAS measurements the main additional noise source was the first mixer which caused the sensitivity to be about 3 times lower than expected from the RNT alone, while major differences have been found for different mixer units.

### 3.12. Improvement of Spectra

The two spectra displayed in Figure 5 illustrate the effect of the THOMAS instrumental changes described above. Especially the major increase in the signal–to–noise ratio by about a factor of 5 and the spectral resolution by about a fac-

tor of 2 are evident. The shift in frequency channels of the DSB spectra is due to a different alignment of the AOS.

### 3.13. Geometry and Time Coverage of Atmospheric OH Measurements

The THOMAS observations ranged between 44 ° and 54 ° northern latitude and between 1 ° and 28 ° eastern longitude (central and eastern Europe). The pointing angles of the THOMAS uplooking geometry were 85°, 80°, and 70° from zenith. The choice of the pointing angle is a tradeoff between path length through the lowermost layers that are causing signal attenuation due to water vapor and path length through the middle and upper stratosphere and mesosphere contributing to the OH signal [*Miller et al.*, 1992]. Therefore a lower pointing angle (e.g., 70°) is more favorable in case of high water vapor concentrations above the observer height, that is, for flight altitudes below or inside the tropopause, and a greater pointing angle (e.g., 80°) is more favorable for flight altitudes in the stratosphere.

There have been five measurement flights on 5 days. They covered local solar times (LST) between 0700 and 2000.

## 4. Retrieval Approach and Error Assessment

In general, the nonlinear equation (3) describes the mapping of atmospheric concentration profiles into the spectrum domain as described in section 2.2. The inverse problem is the retrieval of atmospheric concentration profiles from the measured spectrum, which is in general an ill–posed problem; that is, the solution is sensitive to small perturbations in the measurement [*Rodgers*, 1976]. Linearization and discretization yields an ill–conditioned least squares problem. In order to get a physically meaningful solution, additional constraints have to be introduced in the least squares problem.

There are several unknowns to be retrieved from the measured spectrum: First of all, the OH concentration profile. The number density has been shown to be preferable for retrieval instead of the volume mixing ratio because of the smaller altitude dependence causing a better conditioning of the least squares problem [*Schimpf and Schreier*, 1997]. In addition, the $H_2O$ volume mixing ratio has to be determined because of its influence on the damping of the OH signal. In contrast to OH, the volume mixing ratio of $H_2O$ is prefered for retrieval instead of the concentration because of its lower altitude dependency.

Another parameter is the frequency of the first LO specifying the upper and lower sideband frequency scale with respect to each other. As mentioned in section 3.4, the LO frequency is subject to drifts, so that a mean value is determined by the retrieval algorithm. Last but not least, a possible wavenumber shift of the whole spectrum due to AOS drift/misalignment has to be determined.

For the inversions presented here, the atmospheric pressure and temperature input data were derived from preliminary CRISTA data (version P05) (J. Oberheide and M. Riese, personal communication, 1998) measured in the same time period.

### 4.1. Retrieval Algorithm

Phillips–Tikhonov regularization using the L curve criterion for the automatic determination of the regularization parameter [*Hansen*, 1992] is a proper approach to solve the inverse problem in a numerically robust and efficient way, as discussed by *Schimpf and Schreier* [1997] in an atmospheric remote sensing context. The basic minimization condition of the linear Phillips–Tikhonov regularization scheme is given by

$$\min_{\vec{\mathbf{f}}}(\|\mathbf{K}\vec{\mathbf{f}} - \vec{\mathbf{g}}\|^2 + \lambda^2\|\mathbf{L}\vec{\mathbf{f}}\|^2), \tag{5}$$

where $\vec{\mathbf{g}}$ is the measurement, $\mathbf{K}$ is the weighting function or Jacobi matrix, $\lambda$ is the regularization parameter, $\mathbf{L}$ is the regularization operator, and $\vec{\mathbf{f}}$ is the unknown solution of the inverse problem. $\|\mathbf{K}\vec{\mathbf{f}} - \vec{\mathbf{g}}\|^2$ is called the residual norm, and $\|\mathbf{L}\vec{\mathbf{f}}\|^2$ is the constraint norm.

Solving the minimization condition (5) yields a solution depending on $\lambda$

$$\vec{\mathbf{f}}(\lambda) = \mathbf{K}_\lambda^+\vec{\mathbf{g}} = (\mathbf{K}^T\mathbf{K} + \lambda^2\mathbf{L}^T\mathbf{L})^{-1}\mathbf{K}^T\vec{\mathbf{g}}. \tag{6}$$

In order to avoid numerical instabilities in (6) due to explicit matrix products, minimization condition (5) can be solved in a numerical robust way using generalized singular value decomposition (GSVD) [*Van Loan*, 1976; *Anderson et al.*, 1995].

A variety of methods has been suggested to determine the optimum regularization parameter $\lambda$, for example, a priori (based upon experience from previous retrievals) or a posteriori choice (trial and error, e.g., visual inspection of the solution), discrepancy principle, generalized cross validation, or the L curve criterion. The L curve is a double logarithmic plot of the residual versus the constraint norm depending on $\lambda$ and results in an L–shaped function. The corner of the L curve, defined by its maximum curvature, yields the optimal value of $\lambda$.

$\mathbf{L}$ is the martix representation of an operator introducing a smoothness constraint in the retrieval problem. Typical operators are the identity, the first– or second–order derivative, or the Twomey operator [*Twomey*, 1977]. The Twomey operator asks for minimal deviation of the resulting profile from its mean value. The proper choice of regularization operators $\mathbf{L}$ depends on the actual problem and can be determined by retrievals of simulated spectra with different regularization operators. One criterion for a convenient operator is the sharpness of the L curve corner. In regions with few altitude information contents in the spectrum and where the solution is expected to be constant, the Twomey operator is suitable for the retrieval.

In general, the solution $\vec{\mathbf{f}}(\lambda)$ of an ill–posed inverse problem has a limited altitude resolution, which can be described by an averaging of the true atmospheric profile $\vec{\mathbf{f}}_t$

$$\vec{\mathbf{f}}(\lambda) = \mathbf{A}\vec{\mathbf{f}}_t = \mathbf{K}_\lambda^+\mathbf{K}\,\vec{\mathbf{f}}_t. \tag{7}$$

The matrix $\mathbf{A}$ is called the averaging kernel and plays a critical role in the intercomparison of model profiles and retrieved profiles.

In the discretized inverse problem the values of the concentration profile $\vec{\mathbf{f}}_{OH}$ and the volume mixing ratio of water vapor $\vec{\mathbf{f}}_{H_2O}$ are given depending on altitude. Together with the parameters of the frequency shifts of the first LO and the whole spectrum, one state vector of unknowns $\vec{\mathbf{f}}$ can be composed. For $\vec{\mathbf{I}}$ representing the measured spectrum, $\vec{\mathbf{I}}(\vec{\mathbf{f}})$ being the discretized fit model, and $\mathbf{K} = \partial\vec{\mathbf{I}}(\vec{\mathbf{f}})/\partial\vec{\mathbf{f}}$ being the Jacobian matrix, (5) can be regarded as one Gauß–Newton type iteration step of the nonlinear problem with

$$\vec{\mathbf{f}} = \mathbf{W}\left( f_{\mathrm{LO}_{\mathrm{shift}}} \quad f_{\nu_{\mathrm{shift}}} \quad \vec{\mathbf{f}}_{OH}^{T} \quad \vec{\mathbf{f}}_{H_2O}^{T} \right)^{T} \tag{8}$$

$$\mathbf{K} = \left( \mathbf{K}^{c}_{\mathrm{LO}_{\mathrm{shift}}} \quad \mathbf{K}^{c}_{\nu_{\mathrm{shift}}} \quad \mathbf{K}^{c}_{OH} \quad \mathbf{K}^{c}_{H_2O} \right) \mathbf{W}^{-1} \tag{9}$$

$$\mathbf{L} = \begin{pmatrix} 0 & 0 & c_{OH}\mathbf{L}_{OH} & \mathbf{0} \\ 0 & 0 & \mathbf{0} & c_{H_2O}\mathbf{L}_{H_2O} \end{pmatrix} \mathbf{W}^{-1} \tag{10}$$

$$\vec{\mathbf{g}} = \vec{\mathbf{I}}(\vec{\mathbf{f}}^{c}) - \vec{\mathbf{I}} + \mathbf{K}\vec{\mathbf{f}}^{c}, \tag{11}$$

where the superscript c indicates the current state in the iteration step. Because of the different order of magnitude of the fit parameters, a diagonal weighting matrix $\mathbf{W}$ was introduced to get a better conditioning of the inverse problem.

The parameters $c_{OH}$ and $c_{H_2O}$ are scalar values constituing the weighting between the constraints described by $\mathbf{L}_{OH}$ and $\mathbf{L}_{H_2O}$. Because of the well–posedness of the determination of the wavenumber shifts, these parameters do not have to be regularized, and the corresponding columns of the matrix $\mathbf{L}$ are zero. For $\mathbf{L}_{OH}$ the identity matrix was chosen because of the sharpness of the L curve corner. Because of the low sensitivity of the spectrum to water vapor above 40 km and its expected constant values in this region, the Twomey–operator is adequate for $\mathbf{L}_{H_2O}$. The parameters $c_{OH}$ and $c_{H_2O}$ are given a priori and have been determined by retrievals on simulated spectra with different $c_{OH}/c_{H_2O}$ ratios.

### 4.2. Retrieval Error Assessment

Several perturbations occur in the measured spectrum which are only known with limited accuracy. Most of these perturbations influence the solution of the inverse problem; that is, they result in errors of the solution. Summing over all perturbations yields the total error of the retrieved parameters.

Depending on their nature, the perturbations can be divided in statistical and systematic error sources; for example, noise in the spectrum typically is a statistical error, whereas a base line offset is a systematic error. Except for the spectral noise, all perturbations can be treated as systematic errors.

The statistical error of the retrieved profile is given by the projection of the statistical error covariance matrix of the measurement vector $\vec{\mathbf{g}}$ to the profile space. Under the assumption of statistically independent, Gaussian distributed noise of the measurements $\vec{\mathbf{g}}$ with a statistical error covariance matrix proportional to the identity matrix, the error covariance matrix is given by

$$\mathbf{C}(\vec{\mathbf{f}}) = \sigma^2\mathbf{K}_{\lambda}^{+}\mathbf{K}_{\lambda}^{+T}, \tag{12}$$

where $\sigma^2$ is the variance of the measurement error.

For the estimation of systematic errors, retrievals on simulated spectra with and without perturbation can be performed, and the difference can be defined to be the systematic error. The total systematic error can be defined to be the square root of the sum of squares of all systematic errors.

The error assessment was performed for an observer altitude of 12 km and an elevation angle of 10°. Pressure and temperature were taken form CRISTA data. Profiles of ozone and water vapor were taken from the AFGL U.S. standard atmosphere. Because earlier results of the MAHRSI experiment showed a significantly lower OH amount in the mesosphere compared to the AFGL OH profile, the mesospheric OH concentration of the AFGL profile was reduced by 50 % for the simulation. Because water vapor, ozone, and continuum emissions are dominant in the observed spectral region, no other gases were considered.

The error sources in the THOMAS results can be grouped in measurement noise, retrieval, atmospheric, spectroscopic, and instrument errors (Table 1). Retrieval errors are the uncertainty in the ratio $c_{OH}/c_{H_2O}$ and the uncertainty in the determination of the optimal regularization parameter. Instrument errors are dominated by the noise of the first mixer, a possible base line offset, and uncertainties in the window transmission due to photon–induced absorption (compare with section 3.2). Spectroscopic errors are uncertainties in the spectroscopic database like linestrength and line width errors. Atmospheric errors are uncertainties in the atmospheric temperature, pressure, and ozone profiles. The pointing error is the uncertainty in the pointing angle adjustment. Pointing jitter as well as errors in the field of view of the instrument are assumed to be negligible.

Errors resulting from base line offset are compensated by the water amount and result in wrong damping of the OH signal. Errors changing the effective line width of the OH triplet, that is, the ILS or the OH pressure broadening parameter error, yield an altitude shift of the OH profile.

Dominant instrumental error sources for the OH column are the measurement noise and errors influencing the damping of the OH signal like the $H_2O$ concentration at low altitudes, a baseline offset, the sideband ratio, and the AOS nonlinearity. Furthermore, a pointing bias due to the pointing mirror adjustment results in a baseline offset like distortion. The error in the determination of the regularization parameter is mainly due to systematic features in the residuals, caused by nonwhite noise components in the THOMAS spectra.

The expected overall error budget amounts to 14 % and 15 % for the 40–90 km and 50–90 km weighted OH column densties, respectively, whereas 24 % are expected for the 30–50 km column densities.

## 5. Inversion Results

The inversion of the measured far–infrared spectra yields robust OH concentrations between about 30 km and 90 km. The resulting profiles can be considered as the true OH altitude profiles smoothed by the averaging kernel (compare with equation (7)). To illustrate the smoothing, Figure 6

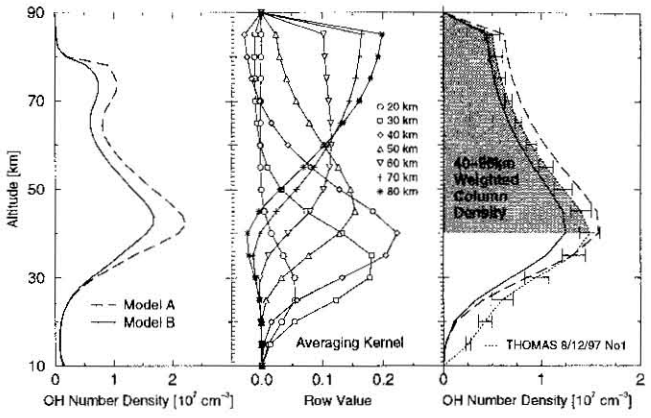


**Figure 6.** (left) OH model profile results using the standard (model A) and a modified chemistry (model B). (middle) A typical set of averaging kernel rows is depicted. The rows are shown every 10 km for clarity. The averaging kernel rows represent the mapping of the high–resolution model profiles to the low–resolution domain of the THOMAS retrieval results. Each row corresponds to a given altitude and represents the contributions of the true OH profile to the value in the inverted profile for the corresponding altitude. The rows are assigned to 15 altitude layers of equal spacing between 15 km and 85 km. (right) Both model profiles smoothed with the averaging kernel so that they can be compared directly to the corresponding profile retrieved from a THOMAS measurement. (Error bars illustrate the statistical error only.) The shaded area represents the weighted column density between 40 km and 90 km.

(left panel) shows two model profiles (1400 LST, August 7, 1997), a typical set of averaging kernel rows (middle panel), and the model profiles smoothed by the averaging kernel (right panel). In addition to the smoothed model profiles, an observed profile (1313 LST, August 12, 1997) is also given. As already mentioned in section 2.2, no altitude information is contained in the measured spectra for altitudes greater than about 50 km, which is also evident considering the shape of the averaging kernel rows. In the middle and upper stratosphere the averaging kernel rows or smoothing functions peak at their corresponding altitude, and their typical width is of the order of 25 km which corresponds to the altitude resolution. In Figure 6 it can also be seen that the norm of the averaging kernel rows is rapidly decreasing with decreasing altitude in the lower stratosphere. This behavior indicates that the information content in the spectra about OH in the lower stratosphere is also rapidly decreasing in this altitude region. This is predominantly due to the fact that the lower stratospheric OH contributes only very little to the detected spectral radiance compared to the noise in the spectrum.

## 6. Comparison With Photochemical Model Results

In this study we use the Naval Research Laboratory (NRL) photochemical model CHEM1D to calculate the mesospheric and upper stratospheric OH abundance profiles for the conditions of the THOMAS observations. This is the same model used in studies of OH data obtained from the

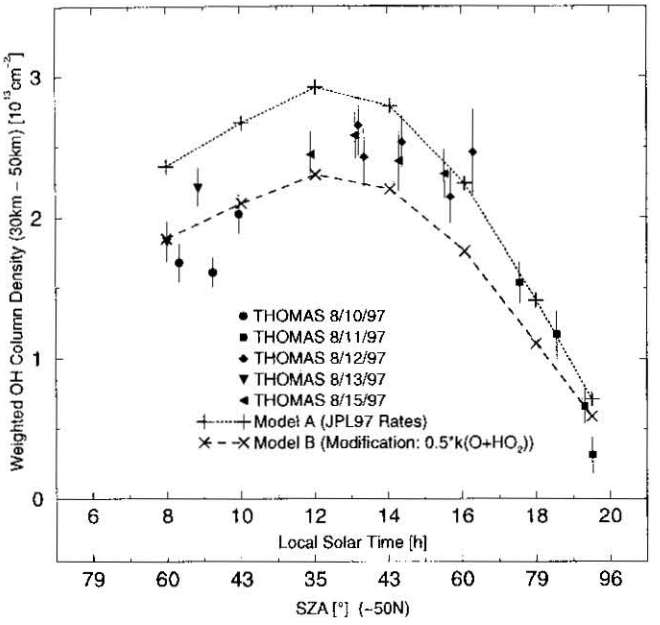


**Figure 7.** Comparison of 30–50 km weighted OH column densities, derived from THOMAS observations and two types of photochemical model calculations.

MAHRSI experiment [*Summers et al.*, 1996; 1997], but updated with more recent chemical kinetics and cross sections [*DeMore et al.*, 1997].

Because of the different altitude resolution, the observed THOMAS OH profiles and the model results cannot be compared directly. Weighted column densities have been chosen for the comparison. They are defined as the integral of the smoothed OH profile between two altitudes. The shaded area in Figure 6 shows the weighted column density between 40 km and 90 km. Figures 7, 8, and 9 show weighted column

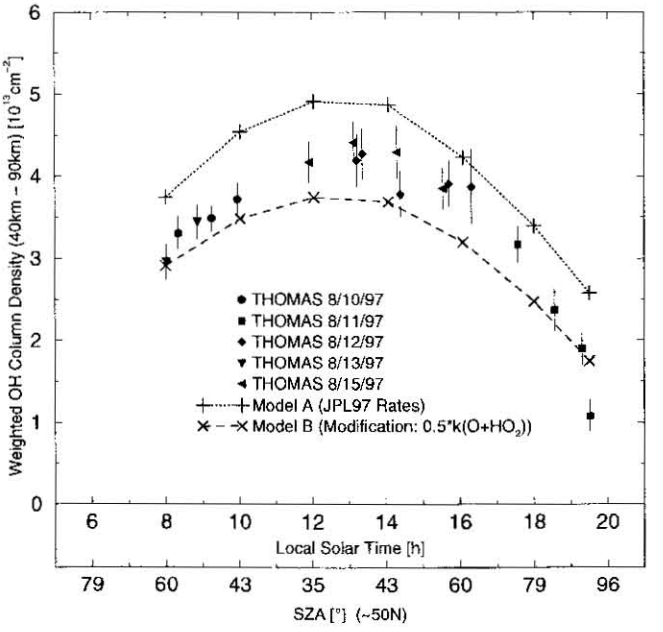


**Figure 8.** Comparison of 40–90 km weighted OH column densities, derived from THOMAS observations and two types of photochemical model calculations.

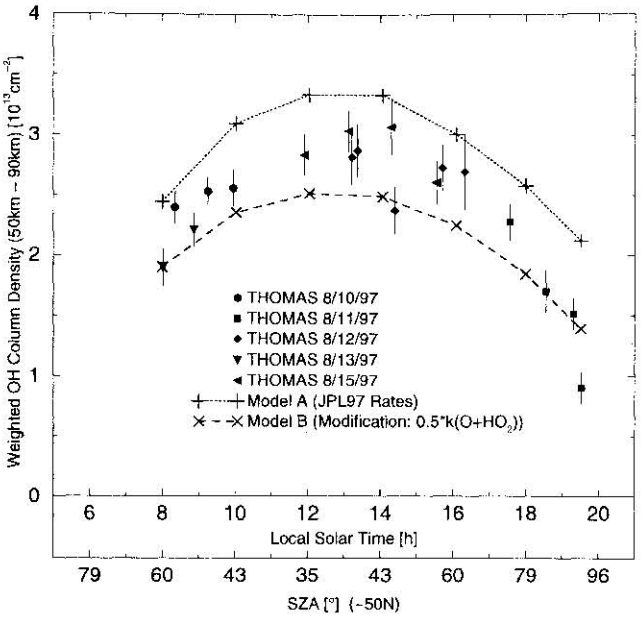


**Figure 9.** Comparison of 50–90 km weighted OH column densities, derived from THOMAS observations and two types of photochemical model calculations.

densities of THOMAS and model calculations for different altitude intervals. The results of all five measurement flights are included in the figures together with the statistical error of the inversion.

For the interpretation of the comparison of measurement and model, one has to bear in mind the possible systematic errors and the significant altitudinal smoothing of the retrieved profile. For the given weighted column densities the sensitivity to OH outside the integrated altitude interval is about 40 % for the 30–50 km column, 15 % for the 40–90 km column, and 20 % for the 50–90 km weighted column amount.

The comparison of weighted OH column densities derived from THOMAS observations and model calculations in Figures 8 and 9 shows that the absolute values of the measured upper stratospheric and mesospheric weighted OH columns generally fall between the standard (model A) and modified (model B) chemistry results; that is, they are about 15 % lower than the predicted values using the standard chemistry. Moreover, all THOMAS observations reflect the shape of the modeled diurnal variation well. Within the experimental uncertainty, no additional influences on OH other than the LST, for example, local or temporal variations in the $H_2O$ abundance, can be identified. The upper stratospheric and mesospheric weighted columns also seem to corroborate the 1994 MAHRSI results that also found an overprediction of OH by standard model calculations in the mesosphere [*Summers et al.*, 1997].

The larger scatter of the stratospheric weighted columns (compare with Figure 7) together with the larger presumed systematic error, makes their clear interpretation difficult. However, the diurnal variation as well as the absolute value of the stratospheric weighted OH columns is well within the range of theory.

## 7. Conclusions

The improved THOMAS instrument was used to measure the thermal emission of atmospheric OH aboard the research aircraft FALCON using uplooking geometry. The instrumental improvements yielded an increase in the signal–to–noise ratio of about a factor of 5 and about a factor of 2 in spectral resolution. Weighted OH column densities between 30 km and 50 km, 40 km and 90 km, and 50 km and 90 km were retrieved using a Phillips–Tikhonov regularization scheme and the L curve criterion for the automatic determination of the regularization parameter. The overall error of these column densities was determined to be 24 %, 14 %, and 15 %, respectively. Comparison of the results to photochemical model calculations using standard chemistry and a 50 % reduction in the rate coefficient for $O + HO_2 \rightarrow OH + O_2$ shows that neither model is capable of reproducing upper stratospheric and mesospheric OH concentrations simultaneously.

**Acknowledgments.** The authors would like to thank T. Weber (DLR) and the CRISTA group (University of Wuppertal, Germany) for their support as well as R. R. Conway (NRL) and M. H. Stevens (NRL) for their advice and cooperation. Furthermore, we would like to thank the DLR flight department and workshop for their excellent cooperation. M. E. Summers was supported by the Office of Naval Research and NASA ACMAP and ITM programs. This work was also supported by DARA/DLR (Bonn).

## References

Allan, D.W., Statistics of atomic frequency standards, *Proc. IEEE, 54*, 221–230, 1966.

Anderson, E., et al., LAPACK users' guide 2nd ed., Soc. for Ind. and Appl. Math. (SIAM), Philadelphia, Pa., 1995.

Anderson, G., S. Clough, F. Kneizys, J. Chetwynd, and E. Shettle, AFGL atmospheric constituent profiles (0–120 km), *Tech. Rep. TR–86–0110*, Air Force Geophys. Lab., Mass., 1986.

Bühler, S., V. Eyring, and H. Küllmann, The impact of continuum emissions in the mm and sub–mm spectral range, final report, contract 10998/94/NL/CN, Eur. Space Res. and Technol. Cent., Noordwijk, Netherlands, 1996.

Burnett, C.R., and K. Minschwaner, Continuing development in the regime of decreased atmospheric column OH at Fritz Peak, *Geophys. Res. Lett., 25*, 1313–1316, 1998.

Carli, B., and J.H. Park, Simultaneous measurement of minor stratospheric constituents with emission far–infrared spectroscopy, *J. Geophys. Res., 93*, 3851–3865, 1988.

Carli, B., M. Carlotti, B.M. Dinelli, F. Mencaraglia, and J.H. Park, The mixing ratio of the stratospheric hydroxyl radical from far–infrared emission measurements, *J. Geophys. Res., 94*, 11,049–11,058, 1989.

Chance, K., W.A. Traub, D.G. Johnson, K.W. Jucks, P. Ciarpallini, R.A. Stanik, R.J. Salawitch, and H.A. Michelsen, Simultaneous measurements of stratospheric $HO_x$, $NO_x$, and $Cl_x$: Comparison with a photochemical model, *J. Geophys. Res., 101*, 9031–9043, 1996.

Chen, L., R. Herschel, D.B. Considine, C.H. Jackman, and J.A. Shorter, Chemical reaction rate sensitivity and uncertainty in a two–dimensional middle atmospheric ozone model, *J. Geophys. Res., 102*, 16,201–16,214, 1997.

Clancy, R.T., B.J. Sandor, D.W. Rusch, and D.O. Muhleman, Microwave observations and modeling of $O_3$, $H_2O$, and $HO_2$ in the mesosphere, *J. Geophys. Res., 99*, 5465–5473, 1994.

Clough, S.A., F.X. Kneizys, and R. Davies, Line shape and the water vapor continuum, *J. Atmos. Res., 23*, 229–241, 1989.

Conway, R.R., M.H. Stevens, J.G. Cardon, S.E. Zasadil, C.M. Brown, J.S. Morrill, and G.H. Mount, Satellite measurements of hydroxyl in the mesosphere, *Geophys. Res. Lett., 23*, 2093–2096, 1996.

Crewell, S., *Submillimeter Radiometrie mit einem flugzeuggetragenem Empfänger zur Messung atmosphärischer Spurenstoffe*, Shaker, Aachen, Germany, 1993.

Crowe, T.W., R.J. Mattauch, H.P. Rser, W.L. Bishop, W.C.B. Peatman, and X. Liu, GaAs Schottky diodes for THz mixing applications, *Proc. of the IEEE, 80*, 1827–1841, 1992.

DeMore, W.B., S.P. Sander, D.M. Golden, R.F. Hampson, M.J. Kurylo, C.J. Howard, A.R. Ravishankara, C.E. Kolb, and M.J. Molina, Chemical kinetics and photochemical data for use in stratospheric modeling: Evaluation number 12, *JPL Publ., 97-4*, 1997.

Englert, C.R., M. Birk, and H. Maurer, Antireflection coated, wedged, single-crystal silicon aircraft window for the far-infrared, *IEEE Trans. Geosci. Remote Sens., 37*, 1997–2003, 1999a.

Englert, C.R., H. Maurer, and M. Birk, Photon-induced far-infrared absorption in pure single crystal silicon, *Infrared Phys. Technol., 40*, 447–451, 1999b.

Englert, C.R., B.A. Schimpf, M. Birk, F. Schreier, R.R. Conway, M.H. Stevens, and M.E. Summers, THOMAS 2.5 THz measurements of middle atmospheric OH: Comparison with MAHRSI observations and model results, in *Atmospheric Science Across the Stratopause, Geophys. Monogr. Ser.*, AGU, Washington, D. C., in press, 2000.

Hachenberg, O., and B. Vowinkel, *Technische Grundlagen der Radioastronomie*, Bibliogr. Inst.–Wiss., Mannheim, Germany, 1982

Hansen, P.C., Numerical tools for analysis and solution of Fredholm integral equations of the first kind, *Inverse Probl., 8*, 849–872, 1992.

Heaps, W.S., and T.J. McGee, Balloon-borne lidar measurements of the stratospheric hydroxyl radical, *J. Geophys. Res., 88*, 5281–5285, 1983.

Heaps, W.S., and T.J. McGee, Progress in stratospheric hydroxyl measurements by balloon-borne lidar, *J. Geophys. Res., 90*, 7913–7922, 1985.

Johnson, D.G., W.A. Traub, K.V. Chance, K.W. Jucks, and R.A. Stachnik, Estimating the abundance of ClO from simultaneous remote sensing measurements of $HO_2$, OH, and HOCl, *Geophys. Res. Lett., 22*, 1869–1871, 1995.

Jucks, K.W., D.G. Johnson, K.V. Chance, W.A. Traub, J.J. Margitan, G.B. Osterman, R.J. Salawitch, and Y. Sasano, Observations of OH, $HO_2$, $H_2O$, and $O_3$ in the upper stratosphere: Implications for $HO_x$ photochemistry, *Geophys. Res. Lett., 25*, 3935–3938, 1998.

Klein, U., *Aufbau und Betrieb eines breitbandigen, bodengestützten Millimeterwellen-Radiometers zur Messung atmosphärischer Spurengase*, Shaker, Aachen, Germany, 1993.

Kraus, J.D., *Radio Astronomy*, McGraw-Hill, New York, 1966.

Liebe, H.J., G.A. Hufford, and M.G. Cotton, Propagation modeling of moist air and suspended water/ice particles at frequencies below 1000 GHz, paper presented at 52nd Specialists Meeting of the Electromagnetic Wave Propagation Panel, NATO Adv. Group for Aerosp. Res. and Dev. (AGARD), Palma de Mallorca, Spain, 1993.

Liou, K.-N., *An Introduction to Atmospheric Radiation*, Academic, San Diego, Calif., 1980.

Miller, S., M. Birk, F. Schreier, and D. Hausamann, Airborne far-infrared heterodyne remote sensing of stratospheric OH: A feasibility study, *Int. J. Infrared Millimeter Waves, 13*, 1241–1268, 1992.

Nitsche, R., Ein quasioptischer 2.5 THz Heterodynempfänger für die flugzeuggestützte Spektroskopie der Atmosphäre, Doct. thesis, Tech. Univ. of Munich, Munich, Germany, 1998.

Osterman, G.B., R.J. Salawitch, B. Sen, G.C. Toon, R.A. Stachnik, H.M. Pickett, J.J. Margitan, J.-F. Blavier, and D.B. Peterson, Balloon-borne measurements of stratospheric radicals and their precursors: Implications for the production and loss of ozone, *Geophys. Res. Lett., 24*, 1107–1110, 1997.

Park, J.H., and B. Carli, Spectroscopic measurement of $HO_2$, $H_2O_2$, and OH in the stratosphere, *J. Geophys. Res., 96*, 22,535–22,541, 1991.

Pickett, H.M., and D.B. Peterson, Stratospheric OH measurements with a far-infrared limb observing spectrometer, *J. Geophys. Res., 98*, 20,507–20,515, 1993.

Pickett, H.M., and D.B. Peterson, Comparison of measured stratospheric OH with prediction, *J. Geophys. Res., 101*, 16,789–16,796, 1996.

Rodgers, C.D., Retrieval of atmospheric temperature and composition from remote measurements of thermal radiation, *Rev. Geophys., 14*, 609–624, 1976.

Röser, H.-P., Heterodyne spectroscopy for submillimeter and far-infrared wavelengths from 100 $\mu$m to 500 $\mu$m, *Infrared Phys., 32*, 385–407, 1991.

Salawitch, R.J., et al., The distribution of hydrogen, nitrogen, and chlorine radicals in the lower stratosphere: Implications for changes in $O_3$ due to emission of $NO_y$ from supersonic aircraft, *Geophys. Res. Lett., 21*, 2547–2550, 1994.

Sandor, B.J., and R.T. Clancy, Mesospheric $HO_x$ chemistry from diurnal microwave observations of $HO_2$, $O_3$, and $H_2O$, *J. Geophys. Res., 103*, 13,337–13,351, 1998.

Schimpf, B., and F. Schreier, Robust and efficient inversion of vertical sounding atmospheric high-resolution spectra by means of regularization, *J. Geophys. Res., 102*, 16,037–16,055, 1997.

Siskind, D.E., and M.E. Summers, Implications of enhanced mesospheric water vapor observed by HALOE, *Geophys. Res. Lett., 25*, 2133–2136, 1998.

Siskind, D.E., B.J. Conner, R.S. Eckman, E.E. Remsberg, J.J. Tsou, and A. Parrish, An intercomparison of model ozone deficits in the upper stratosphere and mesosphere from two data sets, *J. Geophys. Res., 100*, 11,191–11,201, 1995.

Stanley, W.D., Investigation of Allan variance for determining noise spectral forms with application to microwave radiometry, *NASA Contract. Rep. 194985*, 1994.

Summers, M.E., R.R. Conway, D.E. Siskind, R. Bevilacqua, D.F. Strobel, and S. Zasadil, Mesospheric $HO_x$ photochemistry: Constraints from concurrent measurements of OH, $H_2O$, and $O_3$, *Geophys. Res. Lett., 23*, 2097–2100, 1996.

Summers, M.E., R.R. Conway, D.E. Siskind, M.H. Stevens, D. Offermann, M. Riese, P. Preusse, D.F. Strobel, and J.M. Russel III, Implications of satellite OH observations for middle atmospheric $H_2O$ and ozone, *Science, 277*, 1967–1970, 1997.

Titz, R., M. Birk, D. Hausamann, R. Nitsche, F. Schreier, J. Urban, H. Küllmann, and H.P. Röser, Observations of stratospheric OH at 2.5 THz with an airborne heterodyne system, *Infrared Phys. Technol., 36*, 883–891, 1995a.

Titz, R., M. Birk, R. Nitsche, F. Schreier, and G. Wagner, Stratospheric OH measurements with a 2.5 THz heterodyne spectrometer, paper presented at Polar Stratospheric Ozone 1995: The Third European Workshop, Bundesmin. für Bild., Wiss., Forsch. und Tech., Schliersee, Bavaria, Germany, 1995b.

Torr, D.G., M.R. Torr, W. Swift, J. Fennelly, and G. Liu, Measurements of OH($X^2\Pi$) in the stratosphere by high-resolution UV spectroscopy, *Geophys. Res. Lett., 14*, 937–940, 1987.

Twomey, S., *Introduction to the Mathematics of Inversion in Remote Sensing and Indirect Measurements*, Elsevier Sci., New York, 1977.

Urban, J., Messung der stratosphärischen Spurengase ClO, HCl, $O_3$, $N_2O$, $H_2O$ und OH mittels flugzeuggetragener Submillimeterwellen-Radiometrie bei 650 und 2500 GHz, *Ber. Polarforsch. 264*, Alfred Wegener Inst., Bremerhaven, Germany, 1998.

Van Loan, C.F., Generalizing the singular value decomposition, *SIAM J. Numer. Anal., 13*, 76–83, 1976.

Zöger, M., Entwicklung eines flugzeuggetragenen Hygrometers für den Einsatz in der Stratosphäre, *Ber. Forsch. Jülich 3239*, Forsch. Jülich, Jülich, Germany, 1996.

M. Birk, M. Krocka, B. Schimpf, and F. Schreier, Remote Sensing Technology Institute, Deutsches Zentrum für Luft– und Raumfahrt e.V., Oberpfaffenhofen, D–82234 Weßling, Germany. (manfred.birk@dlr.de; michael.krocka@dlr.de; birger.schimpf@dlr.de; franz.schreier@dlr.dc)

C. R. Englert, Upper Atmospheric Physics Branch, Space Science Division, Code 7641, E. O. Hulburt Center for Space Research, Naval Research Laboratory, Washington, D. C. 20375–5352. (englert@uap2.nrl.navy.mil)

R. Nitsche, ISA Industrieelektronik, D–92637 Weiden, Germany. (rnitsche.isa@weiden.de)

M. E. Summers, School of Computational Sciences, Department of Physics and Astronomy, and Center for Earth Observing and Space Research, George Mason University, Fairfax, VA 22030. (msummers@physics.gmu.edu)

R. Titz, Institut für Weltraumsensorik und Planetenerkundung, Deutsches Zentrum für Luft– und Raumfahrt e.V., D–12489 Berlin, Germany. (ruth.titz@dlr.de)

(Received March 14, 2000; revised May 5, 2000;
accepted May 8, 2000.)